

# Impulse Force Generator based on Snap-through Buckling of Robotic Closed Elastica: Analysis by Quasi-static Shape Transition Simulation

Hiromi Mochiyama, Aya Kinoshita, Ryosuke Takasu

**Abstract**—In this paper, we investigate the property of an impulse force generator based on snap-through buckling of a robotic closed elastic rod which is considered as one of good examples of continuum robots. The impulse force generator considered here utilizes a snap through buckling of an elastic rod where its base end is pinned and driven by a rotary actuator forcibly while the tip end is pinned or clamped to the fixed point. One of the most fundamental design problems is to maximize the released elastic energy at each buckling state subject to limited ranges of driving torque and angle of a given actuator. From this design viewpoint, we show two findings obtained from quasi-static planar shape transition simulation of the closed elastica, which will be useful for a design of the robot, that is, the ratio of the elastica length and the endpoint distance decides 1) the buckling angle which relates to the range of an actuator driving angle, and 2) the released elastic energy per the maximum driving torque. We also provide a mathematical description of snap-through buckling based on which we can measure a distance to a buckling point.

## I. INTRODUCTION

Continuum robots have been recognized as one of important research fields in robotics recently. Starting from biologically-inspired motivations [1]–[6], this type of robots is considered to be potentially useful, especially for medical applications [7]–[11]. Our research group has focused on another type of continuum robots which has a function of impulse force generation [12]–[17]. The impulse force generator considered here utilizes a snap through buckling of an elastic rod where its base end is pinned and driven by a rotary actuator forcibly while the tip end is pinned or clamped to the fixed point. This robotic device can be utilized as an artificial muscle of compact mobile robots [12]–[17]. One of the most important design problems of this robotic device is to maximize the released elastic energy at each buckling state subject to limited ranges of driving torque and angle of a given actuator. However, any systematic design procedure has not been provided yet, and design parameters for the robot have been decided by trial and error.

In this paper, we investigate the property of an impulse force generator based on snap-through buckling of a robotic closed elastic rod which is considered as one of good examples of continuum robots. From a design viewpoint, we show two findings obtained from quasi-static planar shape transition simulation of the closed elastica, which will be

H. Mochiyama is with Department of Intelligent Interaction Technologies, University of Tsukuba, Tennoudai 1-1-1, Tsukuba, Ibaraki 305-8573, Japan (mochiyama@iit.tsukuba.ac.jp). A. Kinoshita and R. Takasu were graduate students of University of Tsukuba.

This paper was presented in part at Japanese conferences [22], [23]. This study was supported by a Grant-in-Aid for Scientific Research (B) (No. 22360100) from Japan Society for the Promotion of Science (JSPS).

useful for a design of the robot, that is, the ratio of the elastica length and the endpoint distance decides 1) the buckling angle which relates to the range of an actuator driving angle, and 2) the released elastic energy per the maximum driving torque.

## II. MODELING

### A. Closed elastica as impulse force generator

The closed elastica is a bended elastic strip whose both ends are pinned or clamped to fixed points (Fig.1). The closed elastica is said to be *robotic* if we can apply torques at certain points on the elastica, typically at a pinned end by a rotary actuator so that the elastica can deform actively. By driving the actuator gradually, the elastica deforms gradually, but at some point a drastic shape change of the elastica may occur. This process is called *snap-through buckling*. If we put an object on the way of the shape trajectory around a snap-through buckling state, an impulsive force will be generated at the point of contact between the object and the elastica under snap-through buckling. Therefore, the robotic closed elastica can be utilized for impulse force generation by making use of snap-through buckling.

Although a wide variety of mechanisms of the robotic closed elastica has been already found [12]–[17], we focus on two fundamental planar mechanisms in this paper. One mechanism is called *the planar basic type*, where the base end of the elastica is connected to the axis of an active joint (i.e., pinned and driven by a rotary actuator) while the tip end is connected to the axis of a free joint (i.e., just pinned), and these two joints are perpendicular to the plane on which the backbone curve of the elastica always lies (Fig.2). The other is called *the planar simplest type*. This is almost same as the planar basic type, but only difference is that the tip end is not pinned but clamped with angle  $\phi_{\text{end}}$  from the direction of the line connecting the both ends (Fig.3).

In order to maximize the ability of the robotic closed elastica for impulse force generation, we have to design it so as to maximize the released energy by snap-through buckling subject to limited ranges of an actuator torque and angle. Typical important design parameters of the robotic closed elastica are the size of an elastic strip, i.e., length  $L$ , thickness  $t$  and width  $w$ , and the distance between the both ends of the strip,  $d$ , as shown in Fig.1. Moreover, we choose the way of fixing the tip end, i.e., pinned or clamped. Modeling and simulation of the robotic closed elastica are required for such a design.

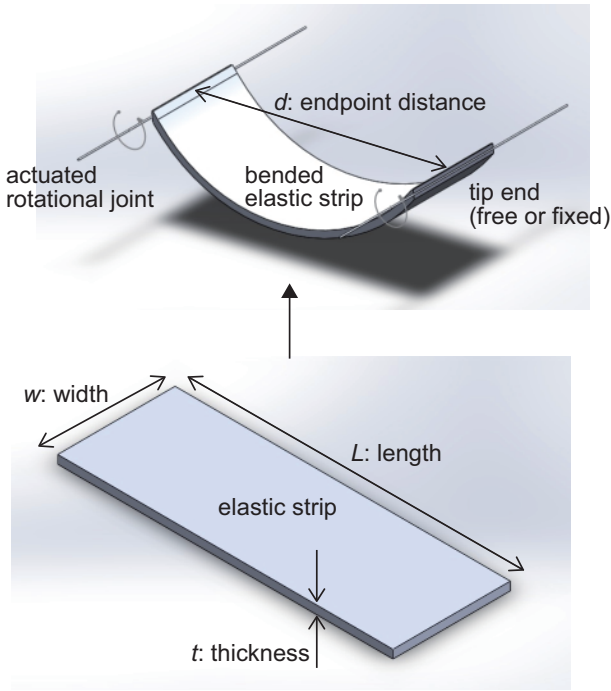


Fig. 1. closed elastica

### B. Kinematics

Consider the Cartesian coordinate frame so as to align the  $x$  axis with the direction of the line from the base end to the tip end of the elastica, and align the  $z$  axis with the direction of the active joint axis. The  $y$  axis is taken such that the coordinate frame is right-handed. Note that, in this coordinate frame setting, the backbone curve of the elastica always exists on the  $x$ - $y$  plane. (See Fig.4 for the case of the planar basic type).

Let  $\sigma \in [0 L]$  be the arc-length parameter, and  $\theta(\sigma) \in R$  the curvature of the backbone curve at  $\sigma$ . It is known that the position vector  $\mathbf{p}(\sigma) \in R^3$  and the orientation matrix of the Frenet frame  $\Phi(\sigma) \in SO(3)$  at  $\sigma$  are governed by the differential equations w.r.t.  $\sigma$  called the Frenet-Serret formula [20]. In the case of plane curves, the solutions can be written by

$$\mathbf{p}(\sigma) = \left[ \int_0^\sigma \cos \phi(\eta) d\eta \quad \int_0^\sigma \sin \phi(\eta) d\eta \quad 0 \right]^T \quad (1)$$

$$\Phi(\sigma) = \begin{bmatrix} \cos \phi(\sigma) & -\sin \phi(\sigma) & 0 \\ \sin \phi(\sigma) & \cos \phi(\sigma) & 0 \\ 0 & 0 & 1 \end{bmatrix} \quad (2)$$

where  $\phi(\sigma) \in R$  is the absolute angle, i.e., the angle of the tangent of the backbone curve at  $\sigma$  from the  $x$  axis. This absolute angle can be expressed by

$$\phi(\sigma) = \int_0^\sigma \theta(\eta) d\eta + u \quad (3)$$

where  $u \in R$  is the absolute angle at the origin. This angle is exactly the control input for changing the shape of the elastica, and is called the base angle.

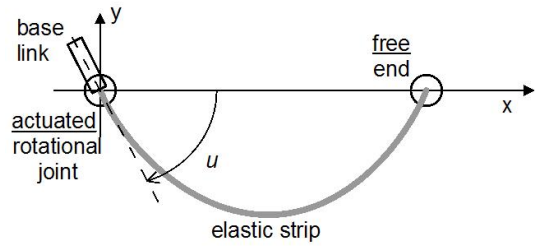


Fig. 2. Planar basic type

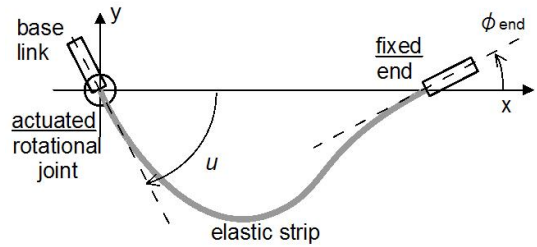


Fig. 3. Planar simplest type

Since the tip position is fixed to the point with distance  $d$  apart from the origin in the  $x$  direction, the following boundary condition should be satisfied:

$$\mathbf{p}(L) = d\mathbf{e}_x \quad (4)$$

where  $\mathbf{e}_x = [1 \ 0 \ 0]^T$  is unit vector in the  $x$  direction. (We also define the unit vectors in the direction of  $y$  and  $z$  axes in the same manner.)

In the case of the planar simplest type, the following boundary condition has to be satisfied additionally:

$$\phi(L) = \phi_{\text{end}} \quad (5)$$

### C. Statics

Based on the elastica theory [18], assume that the elastic rod is unsharable and inextensible, and moreover, satisfies the following constitutive equation which means that the moment at  $\sigma$  is uniformly linear in the curvature :

$$\tau(\sigma) = k\theta(\sigma) \quad (6)$$

where  $k$  is a proportional constant showing the bending elasticity of the rod. The elastic energy stored in the rod,  $E \in [0 \ \infty)$ , can be written by

$$E = \int_0^L \frac{1}{2} k\theta^2(\sigma) d\sigma \quad (7)$$

In the static case, the following Euler equation expressing torque balance <sup>1</sup> holds:

$$k\theta(\sigma) = \mathbf{e}_z^T \{ (\mathbf{p}(L) - \mathbf{p}(\sigma)) \times \boldsymbol{\lambda} \} + \tau_e \quad (8)$$

<sup>1</sup>Equation (8) can be derived by straightforward application of calculus of variation [19]. The detailed derivation can be found in [21] although only Japanese paper is available now.

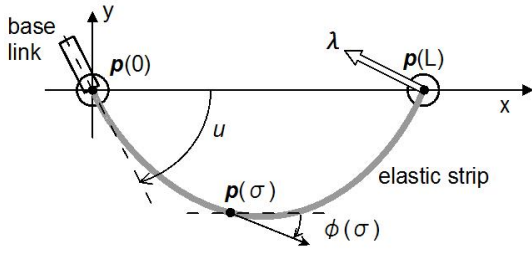


Fig. 4. Geometry of elastica shape on plane

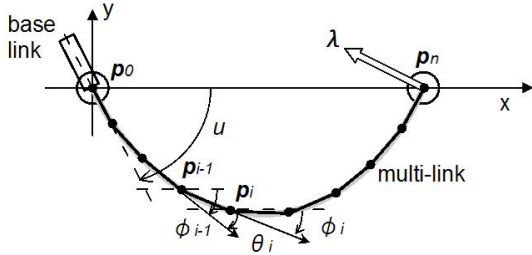


Fig. 5. Multi-link approximation of elastica shape

where  $\lambda \in R^3$  is the constraint force by which the tip position  $\mathbf{p}(L)$  always stays at the point  $de_x$ , and  $\tau_e \in R$  is the constraint torque by which the tip orientation is kept with the angle  $\phi_{\text{end}}$  in the case of the planar simplest case.

Note that  $k$  and the pair of  $\lambda$  and  $\tau_e$  have linear relation for any  $\sigma$  in the balance equation. Therefore, proportional change of  $k$  leads to proportional change of  $\lambda$  and  $\tau_e$ , but does not affect its shape.

To keep the base angle  $u$ , the driving torque by the actuator,  $\tau$ , has to support the elastic moment at  $\sigma = 0$ . Thus,  $\tau$  is written by

$$\tau = -k\theta(0) \quad (9)$$

$$\begin{aligned} &= -e_z^T \{ (\mathbf{p}(L) - \mathbf{p}(0)) \times \lambda \} - \tau_e \\ &= -d\lambda^T e_y - \tau_e \end{aligned} \quad (10)$$

#### D. Discrete Equivalent

Here we consider a discretized model of the closed elastica which will be utilized for numerical simulation and parameter identification and so on.

We approximate a smooth backbone curve of the continuum closed elastica by a polygonal line having  $n$  nodes and links with length  $l = L/n$  (Fig.5). We call this  $n$  the number of partition. These nodes and links are numbered from 0 to  $n$  from the base side. Let  $\theta_i \in R$  be the relative angle from the direction of link  $i-1$  to that of link  $i$ . Then, the position of the  $i$ -th node,  $\mathbf{p}_i \in R^3$ , and the orientation matrix of the  $i$ -th link,  $\Phi_i$ , are given by

$$\Phi_i = \begin{bmatrix} \cos \phi_i & -\sin \phi_i & 0 \\ \sin \phi_i & \cos \phi_i & 0 \\ 0 & 0 & 1 \end{bmatrix} \quad (11)$$

$$\mathbf{p}_i = \begin{bmatrix} \sum_1^i l \cos \phi_i & \sum_1^i l \sin \phi_i & 0 \end{bmatrix}^T, \quad (12)$$

where  $\phi_i \in R$  is the absolute angle from link  $i$  and the  $x$  axis. The relationship between the relative angle and the absolute angle is written by

$$\phi_i = \sum_1^i \theta_i + u \quad (13)$$

where  $u$  is the base angle appear in the continuous model.

Since the position of the tip of the approximated polygonal line,  $\mathbf{p}_n$ , also has to stay at the point  $de_x$ , the following boundary condition should hold:

$$\mathbf{p}_n = de_x \quad (14)$$

Furthermore, in the case of the planar simplest type, since the direction of the tip is also fixed, the following boundary condition has to be satisfied additionally:

$$\phi_n = \phi_{\text{end}}. \quad (15)$$

Notice that if the number of partition,  $n$ , is sufficiently large, we can expect that  $\mathbf{p}_i \approx \mathbf{p}(i \cdot l)$  and  $\theta_i \approx \theta(i \cdot l)$ , because the polygonal line converges to the continuous curve to be approximated. Then, we consider the following discretized torque balance equation:

$$k_d \theta_i = e_z^T (\mathbf{p}_n - \mathbf{p}_{i-1}) \times \lambda + \tau_e, \quad (16)$$

where  $k_d$  is a positive constant corresponding to the bending elasticity  $k$ , and is called the discretized bending elasticity. Note that, for this discretized version of the torque balance equation, the linear relationship between the elasticity and the constrained wrenches still holds. Therefore, change in  $k_d$  does not affect the shape of the discretized closed elastica.

If the number of partition,  $n$ , is sufficiently large, we can also expect that  $k_d \approx k$ . The discrete version of the elastic energy,  $E_d$ , is given by

$$E_d = \frac{1}{2} \sum_1^i k_d \theta_i^2. \quad (17)$$

Furthermore, the driving torque by the actuator is expressed by

$$\tau = -k_d \theta_1 \quad (18)$$

$$\begin{aligned} &= -e_z^T \{ (\mathbf{p}_n - \mathbf{p}_0) \times \lambda \} - \tau_e \\ &= -d\lambda^T e_y - \tau_e. \end{aligned} \quad (19)$$

Therefore, the driving torque is proportional to the bending elasticity in the discrete model as well.

### III. SIMULATION ANALYSIS

Using the discretized model derived in the previous section, we carry out quasi-static shape transition simulation of the closed elastica where equilibrium shapes are calculated for step by step change of the base angle. Based on the simulation, we can see basic properties of the closed elastic useful for designing the impulse force generator, for example,

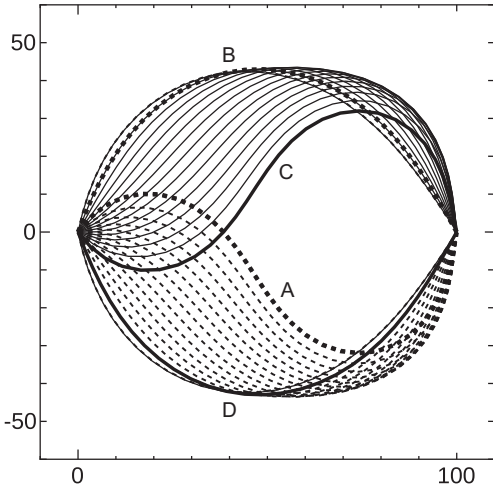


Fig. 6. shape transition of closed elastica for free end

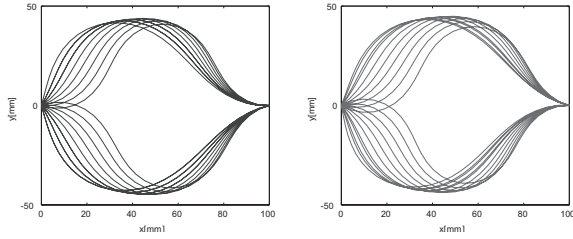


Fig. 7. shape transition of close elastica for fixed end

the released elastic energy at snap-through buckling, the necessary range of the driving angle and so on, although dynamic behaviors, such as motions during snap-through buckling cannot be taken into consideration here.

#### A. Simulation Method

First, we tentatively determine a set of  $\theta_1, \theta_2, \dots, \theta_n$ , the constraint force  $\lambda$ , and the constrained torque  $\tau_e$ . From equation (12), (13), we compute  $\mathbf{p}_1, \mathbf{p}_2, \dots, \mathbf{p}_n$  recursively. Next, we update  $\theta_1, \theta_2, \dots, \theta_n$  by using equation (16) recursively to satisfy the torque balance equation. Third, we obtain the shape of the elastica by computing  $\mathbf{p}_1, \mathbf{p}_2, \dots, \mathbf{p}_n$  from equation (12) again. Then, we update the constrained force and torque according to the errors between  $\mathbf{p}_n$  and  $d\mathbf{e}_x$  and  $\phi_n$  and  $\phi_{\text{end}}$ . We repeat the above process until the errors become sufficiently small, and then increase the base angle  $u$ . In the case of the planar basic type, we do not need to calculate the constrained torque, because we always have  $\tau_e = 0$ .

#### B. Simulation of snap-through buckling

Here we show the result of simulation of shape transition. In this simulation, we set  $k_d = 0.002[\text{Nm}^2]$ ,  $l = 5[\text{mm}]$ . We change the base angle  $u$  with the amount of  $1[\text{deg}]$  from  $-75[\text{deg}]$  to  $75[\text{deg}]$ , and vice versa. Fig.6 is the stick diagram of the shape simulation of the planar basic type for  $d = 100[\text{mm}]$ ,  $L = 140[\text{mm}]$ , with drawing the curves at every  $10[\text{deg}]$  of the base angle. The dashed curves show the

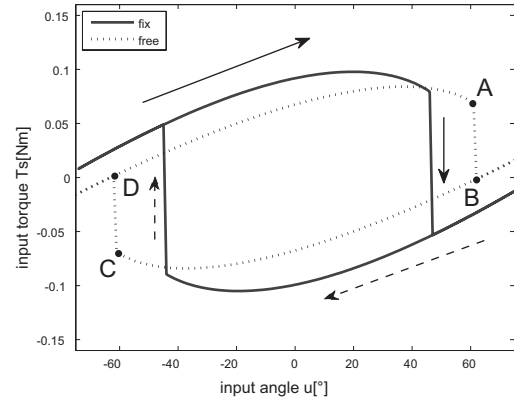


Fig. 8. Driving torque

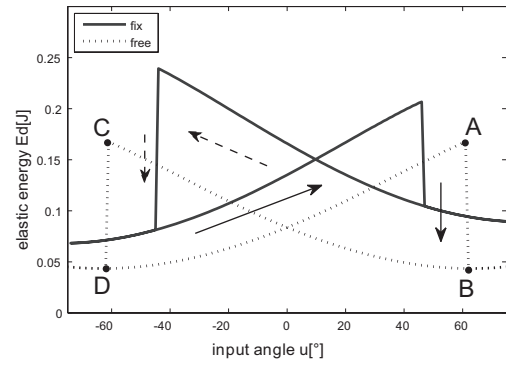


Fig. 9. Stored elastic energy

backbone curves during the upward motion, while the solid curves show the downward one. The four thick curves, A, B, C, and D, in the figure express the shapes just before and after the snap-through buckling. That is, the snap-through buckling occurs from dashed curve A to B upward, and from solid curve C to D downward. We can see that the diagram is symmetric with respect to the x axis.

Fig.7 is the stick diagrams of the shape simulation of the planar simplest type for  $d = 100[\text{mm}]$ ,  $L = 140[\text{mm}]$ ,  $\phi_{\text{end}} = +10[\text{deg}]$ (left) or  $-10[\text{deg}]$ (right), with drawing the curves at every  $15[\text{deg}]$  of the base angle. In this case, we obtain asymmetric diagrams w.r.t. the x axis.

Fig.8 and Fig.9 show the graphs of the necessary driving torque and the stored elastic energy for the base angle change in the case of the planar base type (dashed curves) and the planar simplest type with  $\phi_{\text{end}} = 10[\text{deg}]$  (solid curves), respectively, under the conditions that  $d = 100[\text{mm}]$ ,  $L = 140[\text{mm}]$ . The four point on the dashed curve in each figure, A, B, C and D, correspond to the shapes of curves A, B, C and D in Fig.6. From point A to B, i.e., during the snap-through buckling, for example, sudden drops in the driving torque and stored elastic energy can be seen in these figures. We can also see the change in the necessary driving torque and the stored elastic energy when we change the way to fix

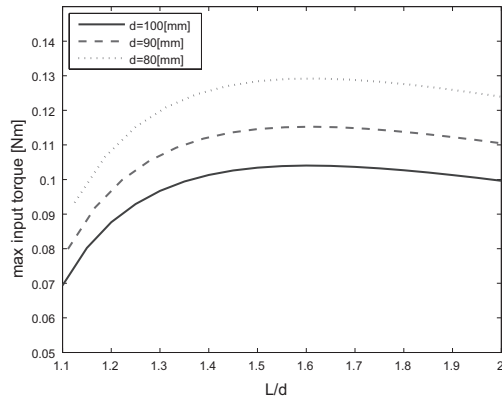


Fig. 10. Maximum driving torque for  $\phi_{\text{end}} = 0$

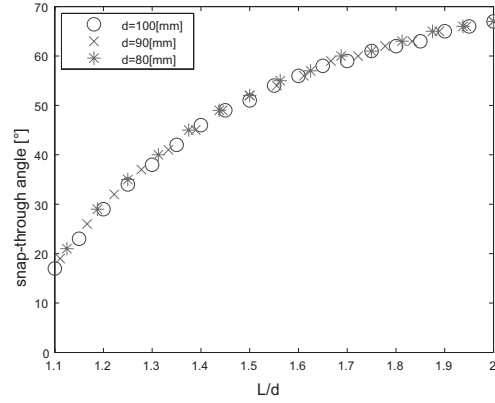


Fig. 12. Snap-through buckling Angle for  $\phi_{\text{end}} = 0$

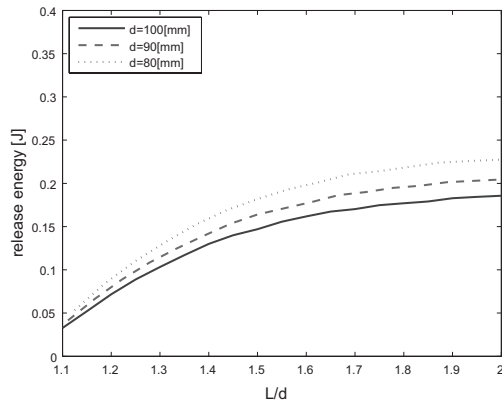


Fig. 11. Released elastic energy for  $\phi_{\text{end}} = 0$

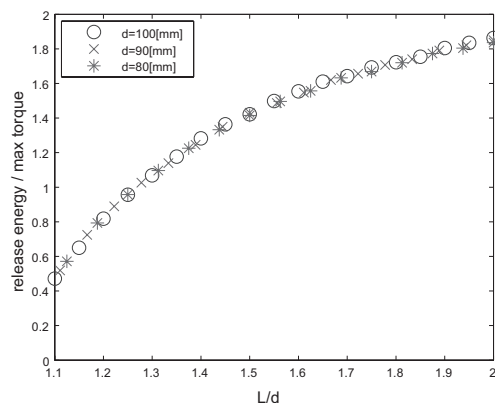


Fig. 13. Ratio of released elastic energy and maximum driving torque for  $\phi_{\text{end}} = 0$

the tip of an elastic strip.

Here note that in this simulation, we do nothing special for simulating snap-through buckling. The drastic shape change can be calculated according to the numerical computation property that it is difficult to find a higher elastic energy solution around the point of snap-through buckling.

### C. Findings from Simulation

Here we focus on the ratio of the elastica length and the endpoint distance  $L/d$ , and the maximum driving torque  $\tau_{\text{max}}$  as well as the angle when the snap-through buckling occurs, and the released elastic energy  $\Delta E$ .

Fig.10 is the graph of the maximum necessary driving torque  $\tau_{\text{max}}$  for  $L/d$ . The horizontal axis means the ratio  $L/d$  while the vertical axis denotes the maximum necessary driving torque  $\tau_{\text{max}}$ [Nm]. The solid, dashed and dotted curves correspond to the conditions  $d = 100, 90, 80$ [mm], respectively. If the ratio  $L/d$  is same, the larger the maximum necessary driving torque is, the smaller the endpoint distance is.

On the other hand, Fig.11 is the graph of the released elastic energy for  $L/d$ . The horizontal axis means the ratio  $L/d$  while the vertical axis denotes the released elastic

energy  $\Delta E$ [Nm]. In this case, the larger the ratio  $L/d$  is, the larger the released elastic energy is.

Fig.13 is the graph of  $\Delta E/\tau_{\text{max}}$  for  $L/d$ . The horizontal axis means the ratio  $L/d$  while the vertical axis denotes the ratio  $\Delta E/\tau_{\text{max}}$ . Plots  $\circ$ ,  $\times$  and  $*$  correspond to the conditions  $d = 100, 90, 80$ [mm], respectively. We can see that the larger ratio  $L/d$  is, the larger the ratio  $\Delta E/\tau_{\text{max}}$  is. Here note that even if endpoint distances are different, all the plots are on the same curve. Therefore, we can say that *the ratio  $L/d$  determines the released elastic energy for the maximum necessary driving torque.*

On the other hand, Fig.12 is the graph of the snap-through buckling angle for the ratio  $L/d$ . The horizontal axis means the ratio  $L/d$  while the vertical axis denotes the snap-through buckling angle. Plots  $\circ$ ,  $\times$  and  $*$  correspond to the conditions  $d = 100, 90, 80$ [mm], respectively. The larger the ratio  $L/d$  is, the larger the snap-through buckling angle is. Here note that, even if endpoint distances are different, all the plots are on the same curve again. Therefore, we can say that *the ratio  $L/d$  determine the snap-through buckling angle.*

We have checked that the above properties are valid for many other parameters.

Our research group has already noticed that  $L/d$  was a very important parameter for the impulse force generator [13]. In this paper, we have succeeded to show the relationship of  $L/d$  to very important quantities for the mechanism design, i.e., the released elastic energy for the maximum necessary driving torque and the snap-through buckling angle, explicitly.

#### IV. MATHEMATICAL REPRESENTATION OF SNAP-THROUGH BUCKLING

In this section, we show a mathematical representation of the snap-through buckling. Without loss of generality, we set  $\tau_e = 0$  for simplicity.

##### A. Nonlinear differential equation to express shape transition

If we fix the base angle  $\phi_0$ , we can find the balanced shape with the corresponding constrained force. Then, we regard the shape and the constrained force as a function of  $\phi_0$ , i.e.  $\theta_i(\phi_0)$  and  $\lambda(\phi_0)$ . For the discretized model,  $\theta_i$  and  $\lambda$  have to satisfy following equations:

$$\begin{aligned} k_d \theta_1 - \mathbf{e}_z^T (\mathbf{p}_n - \mathbf{p}_0) \times \boldsymbol{\lambda} &= 0 \\ k_d \theta_2 - \mathbf{e}_z^T (\mathbf{p}_n - \mathbf{p}_1) \times \boldsymbol{\lambda} &= 0 \\ &\vdots \\ k_d \theta_n - \mathbf{e}_z^T (\mathbf{p}_n - \mathbf{p}_{n-1}) \times \boldsymbol{\lambda} &= 0 \\ -\mathbf{p}_n + d\mathbf{e}_x &= \mathbf{0} \end{aligned} \quad (20)$$

The number of the variables, i.e.,  $\theta_i$  and  $\lambda$  is essentially of  $(n+2)$  because the third (z) element of  $\lambda$  is always zero in planar cases. Here note that this number is equal to the net number of constraints expressed by equation (20) because the last equation is essentially a 2-dimensional constraint for planar cases. In other words, we use the first two equations in the last vector equation in (20) since the third one is always satisfied.

If we differentiate equation (20) with respect to  $\phi_0$ , we obtain the following differential equation about  $\boldsymbol{\theta} := [\theta_1 \ \theta_2 \ \dots \ \theta_n]^T$  and  $\boldsymbol{\lambda}$ :

$$\frac{d}{d\phi_0} \begin{bmatrix} \boldsymbol{\theta} \\ \boldsymbol{\lambda} \end{bmatrix} = \mathbf{g}(\phi_0, \boldsymbol{\theta}, \boldsymbol{\lambda}), \quad (21)$$

where  $\mathbf{g} \in R^{n+2}$  is a nonlinear map characterizing the shape transition. The nonlinear map  $\mathbf{g}$  can be expressed in terms of inner and outer products of physical quantities in space as follows:

$$\mathbf{g} = -\mathbf{S}^{-1} [c_1 \ c_2 \ \dots \ c_n \ \mathbf{b}_1^T]^T \quad (22)$$

$$\mathbf{S} = \begin{bmatrix} \mathbf{A} & \mathbf{B}^T \\ \mathbf{B} & \mathbf{0} \end{bmatrix} \quad (23)$$

$$[\mathbf{A}]_{ij} = \begin{cases} \delta_{ij} k_d + c_j & (i \leq j) \\ c_i & (i > j) \end{cases} \quad (24)$$

$$\mathbf{B} = [\mathbf{b}_1 \ \mathbf{b}_2 \ \dots \ \mathbf{b}_n] \quad (25)$$

$$\mathbf{b}_i = -\mathbf{e}_z \times (\mathbf{p}_n - \mathbf{p}_{i-1}) \quad (26)$$

$$c_i = \boldsymbol{\lambda}^T (\mathbf{p}_n - \mathbf{p}_{i-1}), \quad (27)$$

where  $i, j \in [1, \dots, n]$ ,  $\delta_{ij}$  is the Kronecker delta, and  $\mathbf{S} \in R^{n+2 \times n+2}$  is a block matrix constructed from matrices  $\mathbf{A} \in R^{n \times n}$  and  $\mathbf{B} \in R^{2 \times n}$ .  $[\mathbf{A}]_{ij}$  stands for the  $ij$  element of matrix  $\mathbf{A}$ . Again we ignore the third element of vector  $\mathbf{b}_i$  which is always zero.

Snap-through buckling is a phenomenon that the shape of the closed elastica drastically changes at a certain driving angle. The left-hand side of equation (21) expresses small variation of the shape (i.e.,  $\boldsymbol{\theta}$ , the set of the relative angles) and the constrained force w.r.t. the driving angle. Therefore, we can consider that  $\mathbf{g}$ , which appears in the right-hand side of equation (21), must become very large when snap-through buckling occurs. Since  $\mathbf{g}$  includes the inverse of  $\mathbf{S}$ , it is expected that we can express snap-through buckling by  $\det \mathbf{S} = 0$ , and measure closeness to the point of snap-through buckling by the value of  $\det \mathbf{S}$ .

##### B. Validation from Simulation

We check the value of  $\det \mathbf{S}$  during the shape transition simulation.

Fig.14 is a pair of graphs of  $\det \mathbf{S}$  for the driving angle. In the both figures, the horizontal axis denotes the driving angle and the vertical axis means  $100 \det \mathbf{S}$ . In the upper and lower figures, we increase and decrease the driving angle, respectively. We put some figures of the elastica at the corresponding points on the graphs to show its shapes during the shape transition. From this figure, we can see that the determinant of the matrix changes drastically according to the drastic shape change (around 60 and -60[deg]), which shows the validity of our mathematical representation of snap-through buckling.

#### V. CONCLUSION

In this paper, we showed two properties of the robotic closed elastica important for its mechanism design as an impulse force generator. The properties were found from quasi-static shape transition simulation based on rigorous modeling, kinematics, statics and discretization for the robotic closed elastica. Moreover, we provided a mathematical representation of snap-through buckling which could be utilized for measuring closeness to the point of snap-through buckling.

Here we limited our continuum robot analysis within quasi-static situations. It is necessary to take dynamics into account for precise estimation of generated impulse forces in many applications. Especially, dynamic behavior during snap-through buckling should be analyzed deeply in the future. We are also planning to extend our theoretical analysis to three-dimensional deformation cases where we need to consider twisting of an elastic rod as well as bending. We expect that the theoretical analysis presented in this paper becomes a theoretical footing for these extensions mentioned above and for other types of continuum robots.

#### REFERENCES

- [1] Hirose, S.: Biologically Inspired Robots, Oxford University Press, 1993.

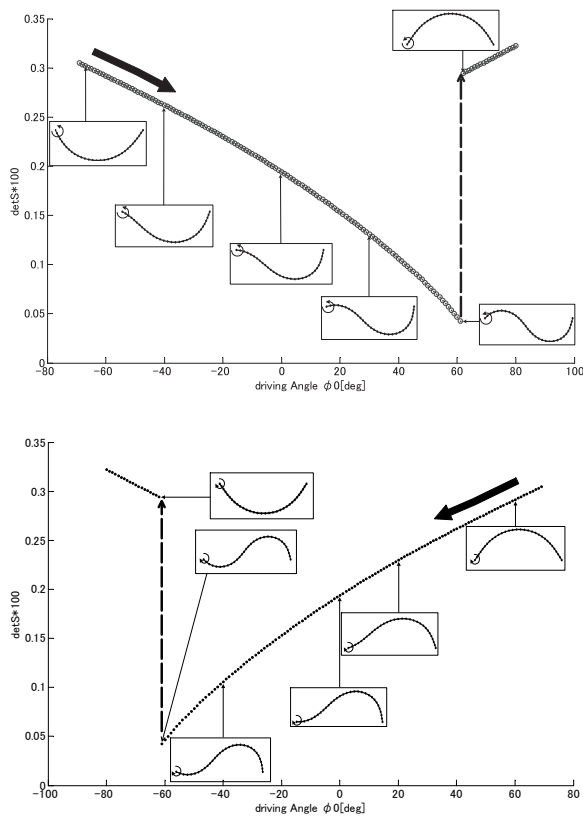


Fig. 14. Relationship between  $\det \mathbf{S}$  and shapes of closed elastica. In the case of the upper figure, we rotate the driving angle  $\phi_0$  in the positive direction (counterclockwise) while in the case of lower figure we do in the negative direction (clockwise).

[2] Suzumori, K., S. Iikura and T. Tanaka: Development of Flexible Micro-Actuator and Its Application to Robot Mechanisms, Proc. of the IEEE International Conference on Robotics and Automation, 1991.

[3] Gravagne, I.A., and I.D. Walker: Manipulability, Force, and Compliance Analysis for Planar Continuum Manipulators, IEEE Trans. Robotics and Automation, 18-3, 263/273, 2002.

[4] Gravagne, I.A., C.D. Rahn and I.D. Walker: Large Deflection Dynamics and Control for Planar Continuum Robots, IEEE/ASME Trans. Mechatronics, 8-2, 299/307, 2003.

[5] Jones, B.A., and I.D. Walker: Kinematics for Multisection Continuum Robots, IEEE Trans. Robotics, 22-1, 43/55, 2006.

[6] Jones, B.A., and I.D. Walker: Practical Kinematics for Real-time Implementation of Continuum Robots, IEEE Trans. Robotics, 22-6, 1087/1099, 2006.

[7] Webster, R.J., J.M. Romano and N.J. Cowan: Mechanics of Precurved-Tube Continuum Robots, IEEE Trans. Robotics, 25-1, 67/78, 2009.

[8] Camarillo, D.B., C.R. Carlson and J.K. Salisbury: Configuration Tracking for Continuum Manipulators with Coupled Tendon Drive, IEEE Trans. Robotics, 25-4, 798/808, 2009.

[9] Simaan, N., K. Xu, W. Wei, A. Kapoor, P. Kazanzides, P. Flint, R. Taylor: Design and Integration of a Telerobotic System for Minimally Invasive Surgery of the Throat, International Journal of Robotics Research (Special Issue on Medical Robotics), 28-9, 1134/1153, 2009.

[10] Mahvash, M., and P.E. Dupont: Stiffness Control of Surgical Continuum Manipulators, IEEE Trans. Robotics, 27-2, 334/345, 2011.

[11] Bajo, A., R.E. Goldman, L. Wang, D. Fowler and N. Simaan: Integration and Preliminary Evaluation of an Insertable Robotic Effectors Platform for Single Port Access Surgery, Proc. of 2012 IEEE International Conference on Robotics and Automation, 3381/3387, 2012.

[12] Mochiyama, H., M. Watari and H. Fujimoto: A Robotic Catapult based on the Closed Elastica and Its Application to Robotic Tasks, Proc. of the 2007 IEEE/RSJ International Conference on Intelligent Robots and Systems (IROS07), 1508/1513, 2007.

[13] Yamada, A., H. Mochiyama and H. Fujimoto: Kinematics and Statics of Robotic Catapults based on the Closed Elastica, Proc. of the 2007 IEEE/RSJ International Conference on Intelligent Robots and Systems (IROS07), 3993/3998, 2007.

[14] Tsuda, T., H. Mochiyama and H. Fujimoto: A Compact Kick-and-Bounce Mobile Robot powered by Unidirectional Impulse Force Generators, Proc. of the 2009 IEEE/RSJ International Conference on Intelligent Robots and Systems (IROS09), 3416/3421, 2009.

[15] Tsuda, T., H. Mochiyama and H. Fujimoto: Robotic Jerboa: A Compact Bipedal Kick-and-Slide Robot powered by Unidirectional Impulse Force Generators, Proc. of the 2010 IEEE/RSJ International Conference on Intelligent Robots and Systems (IROS10), 2523/2524, 2010.

[16] Yamada, A., H. Mameda, H. Mochiyama and H. Fujimoto: A Compact Jumping Robot utilizing Snap-through Buckling with Bend and Twist, Proc. of the 2010 IEEE/RSJ International Conference on Intelligent Robots and Systems (IROS10), 389/394, 2010.

[17] Imai, S., and H. Mochiyama: Basic Performance of Flat Kick-swimming Robot Powered by Impulse Force Generator with Spatially-deformable V-shape Elastica, Proc. of the 15th International Conference on Climbing and Walking Robots and the Support Technologies for Mobile Machines (CLAWAR 2012), 297/304, 2012.

[18] Antman, S.: Nonlinear problems of elasticity, Springer, 1995.

[19] Gelfand, I.M. and S.V. Fomin: Calculus of Variations, translated and edited by R.A. Siverman, Dover Publication Inc., 2000.

[20] O'Neill, B.: Elementary Differential Geometry, Revised 2nd ed., Academic Press, 2006.

[21] Mochiyama, H.: Theory of Robotic Closed Elastica: Approach from Calculus of Variation, Proc. of the 10th SICE System Integration Division Annual Conference (SI2009), 636/639, 2009. (in Japanese)

[22] Takasu, R., and H. Mochiyama: Modeling of Shape Transition of Impulse Force Generator based on Closed Elastica, Proc. of the 12th SICE System Integration Division Annual Conference (SI2011), 0233/0236, 2010. (in Japanese)

[23] Kinoshita, A., and H. Mochiyama: Design of Impulse Force Generator based on Snap-through Buckling of Robotic Closed Elastica, Proc. of the 17th Robotics Symposia, 2011. (in Japanese)